Automated co-registration and calibration in SfM photogrammetry for landslide change detection

M. V. Peppa[a], J. P. Mills [a], P. Moore [a], P. E. Miller [b], J. E. Chambers [c]

[a] School of Engineering, Newcastle University, Newcastle upon Tyne, UK – (maria-valasia.peppa, jon.mills, philip.moore)@ncl.ac.uk

[b] The James Hutton Institute, Aberdeen, UK - pauline.miller@hutton.ac.uk

[c] British Geological Survey, Keyworth, Nottingham, UK - jecha@bgs.ac.uk

Abstract

Landslides represent hazardous phenomena, often with significant implications. Monitoring landslides with time-series surface observations can indicate surface failure. Unmanned aerial vehicles (UAVs) employing compact digital cameras, in conjunction with Structure-from-Motion (SfM) and Multi-View Stereo (MVS) image processing approaches, have become commonplace in the geoscience research community. These methods offer relatively low-cost, flexible solutions for many geomorphological monitoring applications. However, conventionally ground control points (GCPs) are required for registration purposes, the provision of which is often expensive, difficult or even impracticable in hazardous and inaccessible terrain.

In an attempt to overcome the reliance on GCPs, this paper reports research that has developed a morphology-based strategy to co-register multi-temporal UAV-derived products. It applies the attribute of curvature in combination with the scale-invariant feature transform algorithm, to generate time-invariant curvature features, which serve as pseudo GCPs. Openness, a surface morphological digital elevation model derivative, is applied to identify relatively stable ground regions from which pseudo GCPs are selected. A sensitivity threshold quantifies the minimum detectable change alongside unresolved biases and misalignment errors. The approach is evaluated at two study sites in the UK, firstly at Sandford with artificially induced surface change and secondly at an active landslide at Hollin Hill, with multi-epoch SfM-MVS products

This article has been accepted for publication and undergone full peer review but has not been through the copyediting, typesetting, pagination and proofreading process which may lead to differences between this version and the Version of Record. Please cite this article as doi: 10.1002/esp.4502

derived from a consumer-grade UAV. Elevation changes and annual displacement rates at dm-level are estimated, with optimal results achieved over winter periods. The morphology-based co-registration strategy resulted in relative error ratios (i.e. mean error divided by average flying height) in the range of 1:800-2500, comparable to those reported by similar studies conducted with UAVs augmented with real time kinematic (RTK)-Global Navigation Satellite Systems. Analysis demonstrates the potential of the morphology-based strategy for a semi-automatic, and practical co-registration approach to quantify surface motion. This can ultimately complement geotechnical and geophysical investigations and support the understanding of landslide behaviour, model prediction and construction of measures for mitigating risks.

Keywords: UAV, Structure-from-Motion, registration, landslides, curvature

Introduction

Landslides are hazardous phenomena that can have disastrous impacts, involving loss of life as well as damage to infrastructure and communities that yields significant economic implications worldwide (Haque et al., 2016). Reliable approaches to interpret, monitor and mitigate landslide-related hazards are therefore crucial. Traditionally, geotechnical and geophysical ground-based investigations have been used to monitor internal landslide structure (Uhlemann et al., 2016). However, some of these approaches involve invasive sampling, and all require physical access to the site (Chambers et al., 2011), which can be impractical and potentially hazardous. Time-series surface observations can aid quantification of the landslide geometry and kinematics, complement the aforementioned approaches and provide an early indicator of instability (Scaioni et al., 2014), thereby accelerating landslide investigation and prediction. In order to derive suitable time-series of morphological change an appropriate monitoring strategy must be implemented. The choice of strategy depends on various factors, including: a) the type of landslide, its movement mechanism and velocity (Cruden and Varnes, 1996); b) the required spatio-temporal resolution of observation to determine the magnitude of the surface change; c) constraints such as site extent, accessibility, vegetation and weather conditions; d) operational costs of monitoring equipment and logistics (Scaioni et al., 2014; Dall'Asta et al., 2017).

Point-based monitoring techniques, based on Global Navigation Satellite Systems (GNSS) and total stations, together with aerial photogrammetric surveys, are established approaches to derive surface displacements. In the last two decades, airborne laser scanning (ALS) and terrestrial laser scanning (TLS) have become attractive alternatives, enabling generation of high quality digital elevation models (DEMs) (Jaboyedoff et al., 2012). Although offering higher spatial resolution than point-based approaches, ALS and TLS require relatively high financial investment (Travelletti et al., 2012). Further, with static TLS, occlusions can occur due to oblique incidence angles which necessitate the establishment of numerous scanning positions (Jaboyedoff et al., 2012), increasing operational cost. Mobile mapping systems and mini unmanned aerial vehicles (UAVs) equipped with off-the-shelf compact cameras have been rapidly developed over the last decade. These systems alongside the Structure-from-Motion (SfM) and Multi-View Stereo (MVS) processing pipeline, has expedited the automatic generation of high spatio-temporal resolution dense point clouds (Snavely et al., 2008; Remondino et al., 2014), in a time-efficient, cost-effective and user-friendly manner (Fonstad et al., 2013).

The SfM-MVS pipeline is capable of generating a point cloud of tie points (i.e. conjugate image observations) after pixel-based matching, via a self-calibrating bundle adjustment without any *a priori* information on the camera interior orientation parameters (IOPs) (i.e. focal length, sensor size, radial and tangential distortion coefficients). An initial estimate of the focal length is extracted from the exchangeable image file format (Fonstad et al., 2013; Remondino et al., 2014). Scaling and orientation of the resultant point cloud is usually provided by control information in the form of surveyed ground control points (GCPs) via indirect georeferencing (IG), or obtained from the positions/orientations of the camera exposure stations through direct georeferencing (DG). This information, incorporated into a seven-parameter Helmert transformation, determines the reconstructed point cloud and exterior orientation parameters (EOPs) of the taking camera in a fixed reference frame (James and Robson, 2014; Remondino et al., 2014; Carbonneau and Dietrich, 2016). The SfM-MVS pipeline usually results in products comprising a (red green blue) coloured dense point cloud (DPC), a digital surface model and an orthomosaic.

The suitability of the UAV-based SfM-MVS pipeline utilising compact cameras to detect morphological change in various dynamic environments has been presented in numerous studies, for example: landslide monitoring (Niethammer et al., 2012); fluvial dynamics (Woodget et al., 2015; Cook, 2017); soil erosion (d'Oleire-Oltmanns et al., 2012); coastal dynamics (Gonçalves and Henriques, 2015; Turner et al., 2016); glacier monitoring (Immerzeel et al., 2014; Dall'Asta et al., 2017). These studies all demonstrated the flexibility of the SfM-MVS pipeline for monitoring hazardous phenomena, enabling DPCs of several cm ground sample distance (GSD). These studies also reported the variability of the estimated uncertainty (i.e. relevant root mean square errors, RMSEs) of the derived products over stable terrain. Almost regardless of the geo-referencing approach adopted, indirect or direct, SfM-MVS studies invariably report the presence of DEM deformations, such as doming or dishing, causing uncertainties to derived products.

A number of recent studies (James and Robson, 2014; Carbonneau and Dietrich, 2016; Eltner et al., 2016; James et al., 2017a; James et al., 2017b) have investigated the error sources of such deformations. These include: a) poor imaging network geometry; b) low number and poor distribution of GCPs; c) GCPs of low measurement accuracy included as weighting information in the self-calibrating bundle adjustment; d) employment of camera models in the SfM-MVS pipeline that were unable to resolve IOPs and EOPs. Carbonneau and Dietrich (2016) demonstrated that these deformations, if unsolved, can propagate into rotational, translational and vertical offsets in the SfM-MVS derived products, creating systematic tilt and/or radial patterns that adversely affect the time-series observations. Such patterns are usually observable for parallel-axes image acquisition and can be significantly minimised when convergent images are also captured (James and Robson, 2014; Wu, 2014). Convergent imagery can be easily configured with rotor, unlike fixed-wing platforms. For that, James and Robson (2014) recommended the inclusion of smooth banked turns to strengthen the imaging network geometry with fixed-wing UAVs. An additional error source is the presence of vegetation, which creates high surface roughness, affecting the photogrammetric outcome (Cook, 2017). In the context of morphological monitoring, it is crucial to account for these errors in order to estimate the true terrain change (James et al., 2017b).

The aforementioned studies employed a wide spectrum of UAV platforms, from in-house manufactured systems equipped with consumer-grade, single frequency GNSS receivers and Micro-Electro Mechanical System-Inertial Measurement Units (MEMS-IMU), to more expensive, survey-grade UAVs integrated with dual frequency GNSS and multiple MEMS-IMU sensors, or augmented with RTK-GNSS (Carbonneau and Dietrich, 2016; Rehak and Skaloud, 2017). Consumer-grade platforms typically deliver precisions of several m for position and several degrees for orientation of the camera exposure stations. Survey-grade instrumentation, meanwhile, is typically capable of dm-level and degree-level positional and angular precision, respectively (Carbonneau and Dietrich, 2016; Gerke and Przybilla, 2016; James et al., 2017b). This inevitably renders survey-grade more reliable than consumer-grade platforms, especially when DG approaches are employed. Nonetheless, for repeated surveys with RTK-integrated UAVs, systematic errors associated with erroneously fixed ambiguity solutions can be propagated into the UAV camera exposure stations (Dall'Asta et al., 2017) and lead to co-registration discrepancies between epochs in reconstructed DEM time-series. Therefore, augmentation of the SfM-MVS pipeline through the inclusion of a few well distributed GCPs is still considered an essential step to simultaneously reduce biases and derive detectable surface changes at the cm-level (Carbonneau and Dietrich, 2016). However, the installation and maintenance of GCP networks for long-term observations is a labour intensive and costly task, as well as potentially hazardous in steep or mountainous terrain.

Apart from IG or DG, co-registration of multi-temporal 3D surfaces is required for quantifying deformations in the natural environment (Wujanz et al., 2016). To handle the co-registration problem, two approaches have been extensively adopted, namely least squares surface matching and iterative closest point (ICP) algorithms. Least squares surface matching has been applied to glacier monitoring (Fieber et al., 2018) and airborne photogrammetric studies (Gneeniss et al., 2015). The ICP algorithm, meanwhile, has been implemented with TLS observations (Wujanz et al., 2016) and SfM-MVS point clouds derived from UAV imagery (Al-Rawabdeh et al., 2016). A major limitation of both approaches is the requirement for a good starting approximation to the transformation parameters between control and matching datasets. For instance, Al-Rawabdeh et al. (2016) refined the coarse orientation from DG with consumer-grade UAV, with the inclusion of GCPs into the typical SfM-MVS pipeline prior to ICP application. Wujanz et al. (2016) incorporated a similar approach to four-points'-congruent-sets (by Aiger et al. (2008)) into an ICP algorithm to establish an initial alignment. Although this was successfully applied to TLS point clouds on a bare earth quarry face, no investigations have been conducted over terrain with heterogeneous texture. To apply this concept to SfM-MVS outputs, human intervention is required to extract corresponding features over subsequent UAV derived orthomosaics. This task can be cumbersome due to illumination variations across epochs, especially over grassy terrain.

To overcome the aforementioned issues in the absence of GCPs over an active landslide area, this study formulates co-registration as a morphology-matching problem, assuming that surface morphology over stable terrain remains the same across epochs. It introduces a semi-automatic workflow to generate "pseudo control" over relatively "stable" terrain for the effective co-registration of time-series DEMs derived from a consumer-grade, fixed-wing mini UAV and SfM-MVS pipeline. This workflow can potentially bridge the gap between the expensive task of physically establishing and repetitively surveying GCPs using an IG strategy, and the use of survey-grade instrumentation in DG. The proposed methodology, entitled Morphology-Based co-Registration (MBR), was developed and tested at an experimental site, where surface change was controlled, and then transferred to an active landslide.

UAV platform and sensors

A consumer-grade fixed-wing Quest-300 UAV was used for all experiments reported in this paper (QuestUAV, 2017). The Quest-300 has a maximum payload of 5 kg and can fly autonomously for approximately 15 minutes via a predefined series of 3D way-points stored in its autopilot software. The post-flight trajectory information is recorded in a log file, including the time-tagged 3D UAV position at 10 Hz. The Quest-300 initially carried a Panasonic Lumix DMC-LX5 compact camera for RGB image acquisition. A new camera case was designed at Newcastle University and 3D printed using British Geological Survey (BGS) facilities, to mount a Sony A6000 compact camera. Gel within the camera cases is used for vibration damping and a simple gimbal for roll axis compensation, enabling close to nadir image capture. Specifications for both cameras are listed in Table 1.

Methodology

Morphology-Based co-Registration (MBR) workflow

The MBR workflow consists of three main stages (Figure 1).

Stage 1: DEM generation of reference and subsequent epochs

In Stage 1, the SfM-MVS pipeline is implemented to create the DEMs for the reference and subsequent epochs. To create the reference E0 DEM, either a minimum number of GCPs can be used for IG, or the DG strategy can be implemented (steps (a) or (b) in Figure 1). To generate subsequent DEMs, only step (b) is followed, providing approximate positions for coarse georeferencing. To generate the DPCs, the SfM-MVS pipeline was implemented in PhotoScan (PhotoScan, 2016). The DEMs at every epoch were generated using the Orientation and Processing of Airborne Laser Scanning data (OPALS) software with the moving planes interpolation technique (Pfeifer et al., 2014) applied to the DPCs from PhotoScan. This technique fits the best tilted plane to the 15 nearest neighbours at each point in the DPC, by minimising the 3D Euclidean distance in a least-squares sense. It was adopted here because it accounts for relatively extreme local surface variations and preserves a faithful representation of the terrain.

Stage 2a: Pseudo-control generation

Stage 2a refers to the generation of candidate pseudo GCPs by implementing the scale-invariant feature transform (SIFT) operator (Lowe, 2004) with a mean curvature grid, a morphological attribute depicting local undulations of a topographic surface (Rigol-Sanchez et al., 2015). The fundamental differential geometry necessary to derive the mean curvature grid from a DEM can be found in Gray (1997), also followed here via OPALS. The SIFT operator is designed for identifying homologous features on optical imagery and is implemented extensively in SfM-MVS software (Snavely et al., 2008). A few studies have adapted the SIFT operator to non-optical images for automatic registration purposes. These include intensity images obtained with ALS datasets (Wang et al., 2012), range images generated from TLS observations (Barnea and Filin, 2008), hyperspectral (Sima et al., 2014), and synthetic aperture radar images (Dellinger et al., 2015). Here, the SIFT implementation identifies homologous key locations of surface structures (candidate pseudo GCPs) using mean curvature grids of multiple epoch-pairs.

SIFT was implemented by adopting a similar processing chain to that described in Snavely et al. (2008). Erroneous correspondences were filtered by applying the random sampling consensus algorithm (RANSAC, Fischler and Bolles (1981)), incorporated into a 2D similarity transformation. Both SIFT and RANSAC were implemented based on the open-source OpenCV python library (Supplementary Material). Stage 2a (Figure 1) was repeated for epoch-pairs of multiple curvature kernel sizes (5x5 to 33x33). This allowed the identification of numerous interest points with different curvature characteristics, incorporating redundancy into the process. A 0.9 pixel RANSAC threshold was chosen, which corresponds to the average error post transformation, indicating sub-pixel accuracy of SIFT implementation. Tests at both study sites showed that a lower RANSAC threshold resulted in a considerably lower number of pseudo GCPs with a sparse distribution, therefore the 0.9 pixel threshold was considered adequate. RMSEs were derived from the residuals for each candidate pseudo GCP computed after the final RANSAC iteration by transforming the points of curvature j into curvature i (Supplementary Material). These were used as markers' accuracy in PhotoScan (accuracy with which a reference point marker has been placed). 2D coordinates of candidate pseudo GCPs were identified in both the reference and subsequent epochs. Corresponding elevation values were then interpolated from the pseudo GCP positions on the corresponding DEMs derived in Stage 1.

Stage 2b: Stable terrain mask generation

A stable/unstable terrain mask was created based on the classification of the study area into regions with smooth/rough surface texture. Due to underlying surface mechanisms, an active landslide area (i.e. failed terrain) has relatively rougher surface topography than a non-failing region (Tarolli, 2014). Unstable terrain can therefore be represented by segmentation based on rough morphological texture, and vice versa (Baek and Kim, 2015). This in turn can be expressed through the morphological attributes of positive and negative openness. These represent the opening angle of a cone fitted to the DEM, as viewed from above or below the surface, respectively (refer to Yokoyama et al. (2002) for a detailed description). Openness grids were computed in OPALS for each epoch j (Ej) (Supplementary Material). Vectorisation tools combined with map-algebra and focal statistics smoothing algorithms in ArcGIS were applied to the grids for generating the final stable terrain masks.

Stage 2c: Co-registration of epoch pairs over stable areas

Stage 2c includes the selection of the final pseudo GCPs for use in co-registration. 3D coordinates of the extracted pseudo GCPs over stable terrain were incorporated into the epoch-pairwise self-calibrating bundle adjustment, implemented in PhotoScan. Given the established coarse alignment from Stage 1, the coordinates of pseudo GCPs at epoch i (Ei) can be automatically located on each image of the UAV photogrammetric block (Figure 1). Then, the self-calibrating bundle adjustment refines the camera's IOPs - focal length, principal point, radial (three) and tangential (two) distortion parameters. These parameters were chosen as they have been shown to reduce DEM deformations (James et al., 2017a), when tested with a similar compact camera.

After bundle adjustment, the residuals of the pseudo GCPs were estimated, alongside their mean and standard deviation (σ). The latter denotes an unbiased estimator of the sample variance, σ^2, expressing the precision of the automatically generated pseudo GCPs. A statistical outlier test based on the normalised residuals and 95% confidence level (2σ) was used to reject outliers. The number of iterations depended on two criteria, namely a) RMSEs of the XYZ residuals of inlier pseudo GCPs were lower or equal to the DEM spatial resolution; and b) at least one pseudo GCP was completely inside each of five Thiessen polygons used to sub-divide the area of interest. These criteria were determined following performance testing the UAV system under various GCP configurations at Cockle Park, Newcastle University's farm, prior to the two case studies. The tests showed that a minimum number of five well-distributed GCPs could provide a 3D accuracy of approximately 1 x GSD (four GCPs at the periphery and one in the centre of the area of interest, as seen in Peppa et al. (2016)). A similar GCP configuration was also suggested by Reshetyuk and Mårtensson (2016). Such establishment GCP network is a trade-off between fieldwork time and optimal accuracy. Based on this, five Thiessen polygons (each defines the region of influence around a theoretical GCP) were used to verify a reliable pseudo GCP distribution. Any remaining systematic directional errors were manually checked and removed based on the calculation of their azimuth and creation of polar plots. The latter show the azimuthal distribution across the quarters of the polar spectrum, thereby allowing inspection of a dominant direction. The final step of the MBR workflow was to reconstruct the DPC, DEM and orthomosaic per epoch, which was performed in PhotoScan and OPALS.

Stage 3: Sensitivity of surface change

Before quantifying elevation and planimetric surface changes from the co-registered time series, it is important to determine the level of detail that can be achieved with the adopted methodology (Cook, 2017; James et al., 2017b). For that a 3D sensitivity statistic of the surface change was computed. This sensitivity quantifies the minimum detectable change and simultaneously reflects possible biases. Quality indicators of SfM-MVS products constitute the 3D RMSEs at independent check points (CPs) and RMSEs derived from a direct comparison between SfM-based DPC and TLS observations. The first entails sparse and the latter dense point distributions with their corresponding advantages/constrains (point-to-point versus point cloud-to-point cloud comparison). As noted in recent SfM quality studies (e.g. Carbonneau and Dietrich (2016); James et al. (2017b)), a small number of poorly-distributed CPs could not support a spatial distribution analysis of systematic errors. Here, a cloud-to-cloud comparison was undertaken in CloudCompare with the aid of the M3C2 tool, as described in Lague et al. (2013).

The sensitivity level was derived by applying a classical error propagation to the MBR-based point clouds between reference E0 and any other epoch i, for a 95% confidence level (Brasington et al., 2003; Lane et al., 2003), using two equations:

$$s_1 = t\sqrt{e^2_{geor(0)} + e^2_{geor(i)}} \quad (1)$$

$$s_2 = t\sqrt{e^2_{geor(0)} + e^2_{co-reg(i)}} \quad (2)$$

where e_{geor} indicates the 3D RMSE at CPs, with $e_{co-reg(i)}$ denoting the RMSE calculated from the cloud-to-cloud M3C2 distances and $t = 1.96$, the critical value for 95% confidence. The M3C2 comparison was computed after applying a co-registration of epochs over stable terrain with respect to the reference E0. The co-registration algorithm adopted here is the six-parameter rigid transformation ICP (3 translations and 3 rotations), as implemented in OPALS. It should be noted that s_1 refers to sensitivity with respect to RMSEs at CPs (few points) and s_2 refers to sensitivity based on ICP (dense points for M3C2 comparison). The maximum value of s_1 and s_2 was adopted to characterise the lowest detectable surface change. DEM and volume differences were generated with the aid of the Geomorphic Change Detection toolbox (Wheaton et al., 2010), operated in ArcGIS, excluding from the computations the lowest detectable surface change.

Experiments

Three experiments were conducted, each using an identical number of acquired images and flight lines, as well as identical PhotoScan settings per study site (based on Peppa et al. (2016)), as follows:

1) The GCP-based experiment followed the IG strategy, including five GCPs in the SfM-MVS pipeline, and was conducted at both study sites;
2) The MBR-GCP based experiment adopted the MBR workflow, with the reference epoch generated from GCP-based SfM-MVS process, and was conducted at both study sites;
3) The MBR-UAV experiment, which implemented the MBR approach excluding the GCPs in the reference epoch, was performed with the Sony camera at the Hollin Hill landslide only. This experiment was conducted to resemble a realistic case of monitoring an inaccessible hazardous environment with a consumer-grade UAV.

To evaluate the MBR-GCP experiments, the results were compared against the GCP-based results as these provided solutions after the input of a minimum number of five GCPs. Together with elevation and volume changes, displacement rates were estimated especially for the GCP-based and MBR-GCP experiments at the Hollin Hill landslide. 2D positions of 27 sample points, manually identified on subsequent orthomosaics across the site, were calculated for both experiments. The results were cross-validated against independently surveyed GNSS markers.

Sandford Industrial Park test site

Study site and fieldwork

The first two experiments were conducted at Sandford Industrial Park in Shropshire, UK (52°54'26.52"N, 2°37'55.30"W) with datasets acquired on 1st December 2016. This site comprises controlled earthworks acquired for Health and Safety training. The site is an embankment of approximately 20° slope and a relatively flat field of mostly bare soil with sparsely distributed low grass of approximately 0.1 m height. To create artificial surface change, ground materials were excavated from the embankment and placed at the foot of the slope (Figure 2). This area of artificial slope failure covered approximately 100 m^2 and was generated over two epochs. The artificial failure extended 3.50 m along and 6.50 m across the slope with an approximate depth of 0.25 m in epoch E1, and an approximate length, width and depth of 6.50 x 9.50 x 0.50 m in epoch E2 (Figure 2). The surroundings of the synthetically generated change were stable throughout the day, with the exception of the hatched polygon in Figure 2. This was to allow access to excavators and hence, on health and safety grounds, no ground-based observations were performed in this area.

15 black and white circular targets were deployed with a 0.40 m diameter, each equal to approximately 10 pixels on imagery acquired from 120 m flying height. These were observed in GNSS rapid static mode delivering mm-level 3D accuracy relative to a local base station of 0.02 m 3D absolute accuracy in Ordnance Survey Great Britain 36 (OSGB36). TLS observations were surveyed in between excavations for each of the three epochs covering the region bounded in blue in Figure 2.

UAV data acquisition and processing

Three UAV flights were performed before and after the excavations, using the Panasonic camera, with fixed shutter speed of 1/800, fixed aperture of f/2 at the widest angle, ISO 100, 2 s exposure interval, 90% forward and lateral overlap with parallel flight lines and a 120 m predefined flying height.

For the GCP-based experiment, three DEMs were generated at epochs E0, E1 and E2, utilising five GCPs (with indices 5, 6, 8, 9 and 12 Figure 3a). These GCPs were deployed close to the five theoretical GCPs which were used to generate the five Thiessen polygons supporting the examination of pseudo GCP distribution (Figure 3a). In all experiments, DPCs and DEMs of a 0.044 m spatial resolution were constructed.

In the MBR-GCP experiment, 1565 candidate pseudo GCPs (light blue circles in Figure 3b) were detected at locations of slope variations at the foot of the embankment, at the edges of storage units, roofs, fences, machines and over bare earth where the excavator's movement formed structures. The SIFT algorithm did not extract points over the slope failure, which was advantageous for the MBR co-registration. Positive and negative openness grids were computed from the E2 DEM within a 75 x 75 pixel radial distance, equivalent to 3.3 m for 0.044 m pixel resolution, adequate to capture the extent of the artificial failure. A threshold of 84°, which is the average openness value for this area, was selected to differentiate the smooth texture for relatively flat terrain from rougher texture over the steeper terrain (green and red polygons in Figure 3b), after a trial and error procedure.

168 pseudo GCPs were finally extracted over smooth terrain (dark blue rectangles in Figure 3b) with sufficient distribution within the Thiessen polygons. However, only a few pseudo GCPs were located in the south as many candidate points on the manmade features and structures were masked out. Following Stage 2c of the MBR workflow, the residuals of the pseudo GCPs for epochs E1 and E2 were separately analysed by statistical testing. The test was iterated until the RMSEs of the pseudo GCPs residuals were lower than the GSD/DEM spatial resolution (0.044 m). The results are summarised in Table 2. The relatively higher mean in E2 is likely to be caused by the low number of pseudo GCPs in the SE (Figure 4b).

Figure 4 depicts the elevation differences, DEM_{MBR} – DEM_{GCP}, plotted at the level of 1σ = 0.030 m, the maximum σ in elevation of the pseudo GCP residuals (Table 2). Elevation differences, exceeding -2σ, were observed around the manmade objects in both epochs. For E1 the elevation differences showed a general linear slope where the MBR overestimated the elevations in the NW and underestimated in the SE (Figure 4a). In E2 the elevation differences were within $\pm 2\sigma$, lower than those of E1, creating a radial pattern with lower differences in the centre of the study area and higher towards the corners (Figure 4b).

The planimetric residuals and error vectors at CPs are also included in Figure 4. In E1, planimetric residuals show a random distribution. However, in E2, a NW directional bias remained even after the removal of pseudo GCPs that showed systematic directional patterns. This is because a single pseudo GCP with the highest error in the south was not removed (Figure 4b), as this weakened the geometric pseudo GCPs configuration. Analysis after removing this pseudo GCP showed that additional rotational errors were introduced in the north, thereby further increasing the vertical offsets observed in the elevation differences between GCP-based and MBR-GCP DEMs, at the periphery of the site.

Results: Sensitivity estimations

Table 3 summarises the statistical results of the comparison between GCP-based and MBR-GCP solutions at CPs and after the cloud-to-cloud M3C2 distances and ICP registration. The MBR workflow delivered identical mean e_{geor} and $e_{co\text{-}reg}$ for the two epochs, lower than the DEM spatial resolution (0.044 m). For the GCP-based results, the e_{geor} values were approximately half the $e_{co\text{-}reg}$ values. This is possibly attributed to the relatively small number and sub-optimal distribution of the 10 CPs (Figure 3a). A direct comparison between TLS and GCP-based and MBR-GCP point clouds were also conducted. RMSEs of this comparison based on the cloud-to-cloud M3C2 distance calculation are reported in Table 3. The differences between these RMSEs and the $e_{co\text{-}reg}$ values over all epochs were statistically insignificant given the DEM spatial resolution. Table 3 also reports the two sensitivities s_1 and s_2 per experiment, based on Eq. 1 and 2. All sensitivities are comparable in magnitude. The maximum value, rounded to 0.12 m, quantifies the lowest detectable 3D surface change in absolute units for both experiments.

Results: Elevation and volume changes

Elevation differences and volume changes of epoch pair E2-E0 were computed over the slope failure and cross-validated with TLS observations, after excluding occluded areas generated from E2 TLS observations and the ±0.12 m sensitivity level. Computational results are shown in Table 4 and Table 5.

As evidenced in Table 4, statistics of elevation differences show consistency, regardless of the absence/presence of GCPs in the derivation of subsequent DEMs. The MBR-GCP results varied within 1.4 x GSD (i.e. 0.062 m) with the exception of the maximum compared to TLS results. TLS observations captured the subtle surface structures formed by the digging bucket (Figure 2). These detailed surface characteristics cannot be modelled with UAV imagery. However, after converting cut and fill values into percentages of the total volume (Table 5), SfM-MVS estimations fell within the range of ± 2 % relative to TLS.

Figure 5 displays the DEM differences of the epoch-pair E2-E0 generated from the GCP-based and the MBR-GCP solutions. The lowest bound of the elevation differences is equal to the ±0.12 m sensitivity level. Erroneous values were observed at the north corner of the region (indicated with (i)), over the manmade structures (indicated with (ii)) and over vegetation (indicated with (iii)) for both workflows. Change was observed in the SW, indicated with (iv) as part of the excavator movement. The same errors were also observed in DEM differences of epoch-pair E1-E0 from both experiments. However, for epoch-pair E2-E0 additional false elevation differences in the SE in the range [-0.30:-0.12 m] (shown with (v) in yellow in Figure 5) were observed in the MBR-GCP results. These are possibly due to rotational errors caused by the low number of pseudo GCPs in the SE (Figure 3b). Rotational variations of the coarse coordinate systems between E2 and E0 epochs could not be entirely resolved by the SFM-MVS workflow using this sub-optimal pseudo GCP distribution and were propagated as deformations into the DEM.

Hollin Hill landslide

Study site and fieldwork

Hollin Hill (54° 6' 38.90” N, 0° 57' 36.84” W), located 11 km west of Malton, North Yorkshire, UK, is a south-facing hillslope of average 12° gradient, with a 50 m elevation difference in the N-S direction. The land has been mostly used for grazing, with irregular grass height across the site, resulting in high surface roughness, especially during spring through to autumn. Hollin Hill has been characterised as an active slow moving earth-slide, earth-flow landslide based on long-term geophysical and geotechnical ground-based investigations (Chambers et al., 2011; Uhlemann et al., 2016; Uhlemann et al., 2017). The authors reported an average 2 m/yr movement rate with episodic movements reaching 3.5 m/yr, mostly triggered by intensive rainfall. Shallow rotational slumps of weak materials at the upper parts of the slope have caused ground subsidence creating scarps. Materials have been successively translated downwards, forming lobes which have intermittently flowed towards the base of the slope. The complex geological and geomorphological characteristics of this site offered a challenging real-world scenario upon which to evaluate the MBR workflow.

Black and white circular targets (identical to those at Sandford) were surveyed in rapid static GNSS mode, delivering mm-level 3D accuracy with respect to a local base station which was established over stable terrain in an adjacent field. This was surveyed in static GNSS mode during every field campaign, delivering an average 2 cm 3D absolute accuracy in OSGB36. Spot heights and sample points on characteristic surface structures across the site were also surveyed for validation purposes. In addition, BGS fieldwork involved RTK-GNSS observations on a monthly-basis at 45 permanently installed wooden markers (Uhlemann et al., 2016), as shown in Figure 6.

UAV data acquisition and processing

Six field campaigns were carried out, as listed in Table 6. For campaigns E0 and E1, the Panasonic camera was set in shutter priority mode with shutter speed of 1/800 s, varying aperture, ISO 400, 60% forward and 40% lateral overlap with an exposure interval of 2.5 s. After establishing the UAV's operational capabilities under different wind conditions, the settings for the last four campaigns (E2, E3, E4 and E5) were changed. The camera was configured identical to those at Sandford, with 60% forward and 70% lateral overlap, using parallel flight lines from two consecutive flights to strengthen the imaging network (Figure 6). The lower number of images over the landslide in E0, compared to the later epochs, is noticeable in Table 6. For E4 and E5, additional flights were conducted using the Sony camera for the MBR-UAV experiment. This camera was set up with fixed aperture of f/4, fixed shutter speed of 1/1600, ISO 250 and 2 s exposure interval.

For the GCP-based and MBR-based Panasonic experiments, six DEMs with 0.06 m spatial resolution were generated. For the GCP-based, MBR-GCP and MBR-UAV Sony experiments, three DEMs with 0.04 m spatial resolution were created. Due to larger sensor size (Table 1), Sony imagery delivered smaller GSD and higher point cloud density (Table 6). All experiments were performed over the region shown in Figure 6, as adjacent fields were subjected to environmental changes (e.g. crop growth) that would adversely affect identification of stable/unstable terrain. All settings of the MBR workflow tested at the Sandford site were also used at the Hollin Hill landslide.

Prior to curvature and openness grids generation, remaining "off-ground" features (e.g. fences, animals, people and cars) were removed using OPALS. Figure 7 displays an example of negative openness generated from the GCP-based Panasonic experiment derived from the E2, E4 and E5 DEMs. The smooth texture of the "stable" terrain around the landslide fissures yielded wide openness angles, whereas the rough texture of landslide patterns corresponded to narrower openness angles. For E2 and E4 the stable terrain mask was smooth and continuous, as shown by red and blue polygons in Figure 7a. For E3 and E5, the presence of longer grass caused high surface roughness around the lobes at the foot of the slope and affected the smoothness of the mask (E5 in Figure 7b). Figure 7c and d present two examples of mean curvature grids derived with kernel size of 25x25 for epoch E0 and E4 respectively. Within this period, different curvature values were observed over failing parts of the landslide, unsuitable for pseudo GCPs. The locations of final pseudo GCPs selected for epoch pair E0-E4 represent features outside of the main landslide bodies, but with distinctive surface characteristics over the smooth terrain. For example, ridges on the surface in the N-S direction were structured from old hedgerows that were removed before the UAV surveys (Figure 7c and d).

Statistics of the final pseudo GCPs after systematic directional error inspection are shown in Table 7. For the MBR-GCP Panasonic experiment, the vertical RMSEs were lower than the planimetric, with a maximum value of 0.03 m for E1-E4. The highest RMSEs, equal to 0.05 m in Easting and Northing, were observed at E5, still lower than the 0.06 m DEM spatial resolution. For the two Sony experiments, the number of pseudo GCPs is significantly lower than the Panasonic experiment, being extracted from a single epoch pair E4-E5. However, the RMSEs are comparable in magnitude in all experiments. Further analysis of the Panasonic experiment showed that approximately 50% of the pseudo GCPs detected in E2, E3 and E4 separately, were identical to the points used in E5. Even 40% of the E1 detected points was maintained in E5. This indicated that SIFT identified adequate surface features with stable curvature characteristics across epochs.

Figure 8 depicts the planimetric error vectors of pseudo GCPs and CPs, as calculated by the MBR workflow. The vectors are plotted over elevation differences, which were obtained by subtracting the MBR-GCP DEM from the GCP-based DEM at each epoch. Various deformation patterns were observed in across all epochs. For example, in the Panasonic experiment a bowl-shape pattern is shown in E1 and E2 (Figure 8a and b), while a tilt is apparent in E5 with lower deformations in the north and higher in the south (Figure 8e). The error vectors at CPs, in E4 and E5 (Figure 8d and e) show a generally dominant N-S direction. Nevertheless, the error vectors of pseudo GCPs provide a random error distribution without showing dominance towards any particular direction. Among all epochs, E3 (Figure 8c) shows the smallest vertical deformation magnitude across the site with a relatively random planimetric directional distribution at CPs. Between Figure 8e and f, the numerous pseudo GCPs (in Figure 8e) generated a good distribution of control points across site. However, an error might have been introduced because of the epoch-to-epoch transformation resulting in greater planimetric vectors at CPs in the E5 Panasonic when compared to the E5 Sony output.

To understand the presence of bowl-shape deformations in the E1 and E4 epochs, DEMs derived from the GCP-based Panasonic experiment (with 5 GCPs) were subtracted from the DEMs generated from all available GCPs. Based on this DEM differencing, deformations with values ranging within [-0.06-0.03] m were observed, lower than those seen with the MBR workflow in Figure 8a and e. Hence, DEM deformations occurred even with the inclusion of more than five GCPs. As stated by Woodget et al. (2015), such small magnitude deformations are often not reported in studies. The minimal 5-GCP configuration used as reference in GCP-based experiments can be a convenient establishment of control targets, providing a trade-off between fieldwork time and optimal accuracy of approximately 1 x GSD. Moreover, the greater deformation magnitude could also be attributed to the pseudo GCP uncertainties that served as marker accuracies in the SfM-MVS pipeline. James et al. (2017a) observed that vertical RMSEs at CPs increased for larger values of marker accuracies, creating bowl-shape deformations. Even though the uncertainties of the experiments were lower than the GSD, these deformations could be caused by a combination of factors, which are summarised in Discussion.

Results: Sensitivity estimations

Table 8 and 9 summarise the RMSEs derived at CPs and after the M3C2-ICP implementation together with the sensitivities for all experiments. For the GCP-based Panasonic, the $e_{co\text{-}reg}$ across all epochs lie within the range of the e_{geor}. For the MBR-GCP Panasonic, the ICP minimised possible misalignments resulting in smaller values of $e_{co\text{-}reg}$ when compared to the e_{geor}, with the exception of E1 and E5. The higher $e_{co\text{-}reg}$ uncertainties reflect the deformation patterns seen in Figure 8a and e. The E5 $e_{co\text{-}reg}$ uncertainty (i.e. 0.087 m) could also be caused by vegetation change. This is also seen through the openness mask creation that showed rough texture mostly around the lobes (Figure 7b). In the MBR-GCP Panasonic, the E2, E3 and E4 $e_{co\text{-}reg}$ uncertainties have similar magnitudes lower than the 0.06 m DEM spatial resolution. The two sensitivities of the GCP-based Panasonic show consistency, which is not the case with the MBR-GCP Panasonic experiment where s_2 sensitivity indicates unresolved errors.

For Sony datasets (Table 9), E4 was used as a fixed reference surface for ICP. Hence, the statistics cannot be directly compared to results from the Panasonic datasets. All experiments provided $e_{co\text{-}reg}$ and e_{geor} uncertainties that do not differ by more than 0.04 m, equal to the DEM spatial resolution derived from Sony datasets. Moreover, s_2 sensitivity of the MBR-UAV Sony, which does not include the absolute uncertainty, still lies within the bounds of s_1 and s_2 of the MBR-GCP Sony experiment.

Overall, the MBR workflow detected a lowest surface change within 0.088-0.22 m (Table 8). The minimum value, close to the sensitivities of the GCP-based results in both study sites, represents the optimal sensitivity. The maximum value, double the maximum sensitivity estimated from the GCP-based experiment (i.e. 0.109 m), represents the threshold of surface change that can be identified from SfM-MVS outputs that involve biases. The statistics of an independent cross-validation with 559 spot heights surveyed in E5 (Table 10), validate the overall MBR co-registration solution in elevation. Discrepancies between the vertical RMSEs and the 0.088 m minimum sensitivity are insignificant, implying that translational and rotational biases were possibly reflected in the maximum sensitivity.

Results: Displacement rates, elevation and volume changes

Subsequent epoch analysis for estimating change showed that a) planimetric and vertical change lower than the ±0.109 m sensitivity level was observed in the E1-E2, E2-E3 and E3-E4 epoch pairs; and b) the E1-E4 epoch pair produced the clearest picture of landslide elevation differences due to minimal seasonal variations during winter. Figure 9a and b depict the displacement rates estimated from GNSS observations. Figure 9c, d, e and f show the displacement rates and DEM differences between E0-E4 and E0-E5 estimated from both experiments. The start positions are coordinates of E0 for both the 27 sample points and the GNSS pegs. The UAV and GNSS field campaigns did not coincide with the exception of the reference E0 (12/14, Table 6). As there were no GNSS observations for E4 and E5, the displacements were derived by interpolating the corresponding observations from the GNSS campaigns before and after E4 and E5.

Utilising 27 sample points, the E0-E4 and E0-E5 displacement rates between the GCP-based and MBR-GCP Panasonic workflows gave a mean difference of -0.03 m ±0.02 m and -0.05 m ±0.03 m respectively. The MBR-GCP workflow underestimated the movement rate for small magnitudes such as the motion at the western upper part of the landslide (smaller vectors are observed in Figure 9e and f than with GCP-based results in Figure 9c and d). The two workflows provided good agreement in direction of movement. Satisfactory results were also achieved compared to directions derived from GNSS (Figure 9a and b versus Figure 9e and f). Figure 9g verifies the direction of both workflows, by depicting the movement of a crack close to point 100. This movement was delineated with multi-epoch total station observations, in combination with the GCP-based orthomosaics.

Only two out of the 45 wooden markers (4 and 8 shown in Figure 9) could be identified on the Panasonic orthomosaics due to the small size of the markers. With respect to Sony imagery, a 0.02 m GSD allowed for identification of 10 markers on both E4 and E5 orthomosaics. The 3D GNSS coordinates of these 10 markers were interpolated for the dates of E4 and E5 UAV campaigns. A 0.11 m 2D RMSE and a 0.06 m 3D RMSE were computed from the 2D horizontal and vertical differences between GNSS and GCP-based Sony datasets. RMSEs derived from comparison of GNSS against MBR-GCP Sony observations (0.09 m 2D RMSE, 0.05 m 3D RMSE) delivered similar agreement.

As evidenced in Figure 9c, d, e and f surface failure at the back scarp appeared to have occurred after 02/16, indicating an episodic landslide movement. A maximum ground subsidence of approximately -1.70 m was observed, with material sliding down-slope yielding a maximum elevation increase of approximately +1.05 m between epochs E4 and E5. Apart from the western and eastern lobe and the back scarp, the most active parts of the landslide, motion was also observed at GNSS pegs between the two lobes (e.g. peg 33 in Figure 9b). This region was characterised as stable/smooth terrain when generated from the openness mask with the MBR workflow (Figure 7a and b). No surface fissures were apparent on the orthomosaics, thus the smooth characterisation was valid. However, the instability of the subsurface, caused by a combination of hydrogeological factors investigated in Uhlemann et al. (2016), probably resulted in the movement of marker 33. For example, intensive rainfall over long durations could increase soil moisture and pore water pressures, resulting in slope failure. Rotational failures at the back scarp could force material to prograde downwards increasing loading further down-slope thereby generating further instability. This subsurface movement was possibly propagated into the MBR workflow, resulting in a systematic pattern observed at CPs in Figure 8e with a N-S direction similar to the motion direction in Figure 9.

Rainfall observations from a weather station at Hollin Hill, obtained and analysed by BGS (Uhlemann et al., 2017) indicated that there were a comparable wet spring and summer period of 2015 but a relatively wet winter period of 2016. Peg 8 was displaced less than the ±0.109 sensitivity level until the start of the winter 2016 (Figure 9a and c), whereas it was pushed downwards 0.6 m by the failing material from the top of the slope from epoch E4 to E5 (Figure 9b and d). Point 100 was moved approximately 0.16 m until the start of the winter 2016, but it was displaced almost 0.5 m from epoch E4 to E5 (Figure 9g). This activation/reactivation period of the landslide was previously investigated by BGS with multiple-ground-based observations (Uhlemann et al., 2016; Uhlemann et al., 2017). Moreover, the displacement over the lobes were greater than the movement at the top of the slope, even during non-active periods at the end of winter 2016 (Figure 9a, c, and e). Higher movement rates were observed over the eastern lobe after epoch E4 (Figure 9b, d, f and g), possibly triggered by a significant rainfall event at the beginning of winter 2016.

Figure 10 shows the volume changes of significant landslide motion over the back scarp and eastern lobe across selected epoch-pairs (white polygons in Figure 9), excluding the regions with noise due to grass growth (e.g. toe of the slope in Figure 9c and d). A total volume cut of -262.28 m^3 was calculated from GCP-based results. Out of this total, an average -6.95 m^3 difference in volume change (i.e. 3%) between the two workflows was estimated. Similarly, for a 312.48 m^3 total fill volume, an average 24.72 m^3 difference was computed, equivalent to 8%. In the same manner, volume changes were computed between E4-E5 over the back scarp with the GCP-based and MBR-GCP Sony outputs. Overall, a 8.5% difference in volume change between the two workflows was estimated.

Discussion

The MBR workflow implemented the SIFT algorithm alongside the morphological attribute of curvature to generate pseudo GCPs with curvature characteristics invariant through time. This concept can overcome issues associated with optical images such as illumination variations, shadows etc., thereby increasing the effectiveness of the co-registration. As this does not rely on the identification of manmade features, it can be applicable to natural environments, therefore finding favour in the study of remote inaccessible areas. Together with curvature, openness added reliability in selecting pseudo GCPs only over stable terrain, thereby supporting the detection of potential hazards over landslide environments.

Analysis presented in this paper has identified two essential requirements for the MBR workflow: a) the site under investigation should have discrete surface characteristics over stable terrain; b) a heuristic observation procedure is necessary for the determination of the optimal RANSAC threshold, *curvature* kernel sizes used with the SIFT algorithm and directional threshold for removal of dominant systematic errors. These conditions are site dependent requirements that limit the direct transferability of the MBR workflow to any natural environment site and involve human intervention, restricting automation of the MBR workflow. It should also be noted that tests here were applied to a particular landslide type. Other types (e.g. a block slide), might not always result in surface roughness. This suggests that an understanding of the landslide mechanism is required prior to MBR implementation, which might not always be feasible in hostile situations or one without prior ground investigation.

Perhaps the most significant weakness of the MBR workflow, compared to the benchmark SfM-MVS pipeline with five GCPs, is that uncertainties greater than 1 x GSD, propagated through the workflow and caused DEM deformations. These uncertainties reflected translational and/or rotational offsets that remained unresolved from the SfM-MVS workflow that even the ICP algorithm could not remove (e.g. high s_2 values in E1 and E5 in Table 8). The cause possibly stems from a combination of factors: the approximate camera exposure stations derived from the UAV's consumer-grade on-board sensors; the inferior imaging network; the epoch-to-epoch transformation of the SIFT points (Stage 2a in Figure 1); the unstable SfM-MVS solution in relation to marker accuracies and approximate coordinates; vegetation changes; and the actual landslide motion; that were all integrated into the workflow. Most errors are hidden in the SfM-MVS pipeline and only become apparent as DEM deformations (also noted by Carbonneau and Dietrich (2016)). Because of this, generation of a budget per error source is a challenging task. To this end, James et al. (2017a) investigated systematic errors at image-level with dedicated software. Additionally, Eltner and Schneider (2015) suggested that the camera's IOPs, estimated from calibration procedure pre or post UAV surveys, could be used as fixed for subsequent bundle adjustments. This approach could potentially reduce DEM deformations. James et al. (2017b) also introduced multiple Monte Carlo tests to examine the optimal PhotoScan settings (e.g. marker accuracies) and to quantify the precision of the camera's IOPs/EOPs within SfM-MVS processing. However, in this study, the s_2 sensitivity (Equation 2) can constitute a global quality index of the MBR co-registration that accounts for all possible errors, even in the absence of GCPs. Such analytical methods (James et al., 2017a; James et al., 2017b) could be beneficial to the MBR workflow, thereby preventing error propagation in later stages of the monitoring strategy. Moreover, many pseudo GCPs with suitable spatial distribution can offer high redundancy, crucial for bundle adjustment, as well as they can counteract potential inaccuracies caused by the lower reliability of natural SIFT features compared to GCPs especially over grassy terrain.

With respect to spatial resolution, 3D RMSEs at CPs resulting from the GCP-based and MBR Sandford experiments showed general consistency, equal to 1 x GSD. At Hollin Hill, the MBR workflow estimated RMSEs in the region of 1.9-3.3 x GSD and 1-1.6 x GSD for the Panasonic and Sony cameras, respectively. These are comparable to uncertainties reported in previous studies with RTK-UAVs without GCPs. For example, vertical errors of 1.4 x GSD and 2.4 x GSD were derived in Dall'Asta et al. (2017) and Gerke and Przybilla (2016), respectively. Woodget et al. (2015) also reported errors higher than 5 x GSD, caused mostly by vegetation. According to James and Robson (2012) and Eltner et al. (2016), the estimated uncertainties can also be interpreted as relative error ratios (i.e. mean error divided by average flying height). Relative error ratios from MBR results of both study sites lie in the range 1:800-2500, with the lowest ratio attributable to biases in the E5 MBR-GCP Panasonic solution at Hollin Hill and the highest ratio achieved with the E2 MBR-GCP Panasonic solution at Sandford. These ratios are in good agreement to the ratios 1:1600-1900 computed from errors and flying heights reported in two recent studies with RTK-UAVs (Gerke and Przybilla, 2016; Dall'Asta et al., 2017). A 1:1000 ratio, derived from the E5 MBR-UAV Sony solution at Hollin Hill, is comparable to the lower end of the ratios 1:1080-

9400 which were estimated from the use of digital single-lens reflex cameras by James and Robson (2012).

In relation to the artificial surface change induced at Sandford, a ± 0.120 m sensitivity level was detected independently of the presence of GCPs. This corresponds to 2.7 x GSD, setting the uncertainty level of the MBR solution. The volume of change was quantified with ±2 % difference to the TLS datasets. In relation to the Hollin Hill landslide, a ± 0.221 m minimum detectable change was estimated with the MBR-GCP workflow and the volume of change was quantified with ± 8.5 % from the GCP-based solutions. The discrepancies between the two sites are attributable to the uncertainties previously discussed. Moreover, the setup at Sandford was ideally designed to simulate change in the middle of a site surrounded by known stable terrain with little vegetation and data acquired with short revisit time. By comparison, the Hollin Hill landslide constitutes a real world scenario with vegetation producing additional noise. This has been documented as a problematic factor in other SfM-MVS workflows (Woodget et al., 2015; Carbonneau and Dietrich, 2016; Cook, 2017). A higher temporal frequency of UAV acquisitions would confirm the stability of the smooth terrain. This in combination with movement tracking of permanently fixed ground targets could potentially evaluate the sensitivity levels of surface change over smooth terrain. Accounting for the noise due to vegetation variation, winter would constitute the optimal period to conduct UAV surveys over such a challenging site. Constraints due to weather conditions are always essential considerations when planning UAV field surveys during winter.

Conclusions

This paper has proposed a morphology-based co-registration (MBR) strategy to align multi-temporal UAV-derived products for quantifying landslide information, without the usual reliance on ground control information. It applies the openness roughness measure to identify stable surfaces and the SIFT algorithm with curvature grids to automatically extract correspondences in epoch-pairs. These correspondences serve as pseudo GCPs which are incorporated into the SfM-MVS processing pipeline. Unresolved misalignment errors and other possible biases from the co-registration are expressed in the sensitivity level, which quantifies the minimum detectable change and constitutes a quality index of the MBR strategy. Through an error assessment, the study has highlighted that the MBR strategy can produce precisions of a similar scale to those estimated from an IG approach with five GCPs. This outcome can be achieved mostly with periodic observations of a high temporal frequency and over stable regions that are not adversely affected by vegetation changes. The MBR strategy together with a consumer-grade UAV platform, can provide uncertainties comparable to those derived from more expensive RTK-UAVs. On the other hand, the MBR strategy could be subsequently used with RTK-UAV referenced data capable of higher accuracy DEMs and curvature grids compared to consumer-grade UAV-based models. This would potentially offer a monitoring strategy of higher sensitivity level. Risks associated with setting out GCPs and the intensive survey workload of potentially hazardous environments can be significantly reduced, even with consumer-grade UAV referenced data, as seen in the presented experiments.

Thus, the MBR strategy can constitute a potentially time-efficient and cost-effective co-registration solution applicable to inaccessible areas. The MBR strategy can also deliver multi-temporal surface changes that could complement the ground-based geotechnical and geophysical subsurface observations, thereby accelerating investigation and prediction approaches to aid the development of landslide-mitigation measures.

Acknowledgements

This research was jointly funded by a Natural Environment Research Council (NERC) BGS BUFI award (S241) and an Engineering and Physical Sciences Research Council (EPSRC) DTA award (EP/L504828/1). The BGS contribution to this paper is published with the permission of the Executive Director of the BGS-NERC. The authors wish to thank Sebastian Uhlemann of BGS for providing the time-series of GNSS permanent marker observations. The authors also convey their gratitude to Leica Geosystems and the Hawk Group (www.hawk-groupd.co.uk) for their collaboration at the Sandford site, as well as the Hollin Hill landowners for allowing access to their property. Many thanks to Martin Robertson, Elias Berra, Magdalena Smigaj, Polpreecha Chidburee and Ben Grayson, of Newcastle University for fieldwork assistance. The authors would like to thank the two reviewers and the associate editor for their constructive comments and recommendations. Finally, the authors declare that they have no conflict of interest.

References

Aiger, D., Mitra, N. J. and Cohen-Or, D. 2008.4-Points congruent sets for robust pairwise surface registration. *ACM Transactions on Graphics,* 27(3), doi:10.1145/1360612.1360684.

Al-Rawabdeh, A., Al-Gurrani, H., Al-Durgham, K., Detchev, I., He, F., El-Sheimy, N. and Habib, A. 2016. A robust registration algorithm for point clouds from UAV images for change detection. The International Archives of the Photogrammetry, Remote Sensing and Spatial Information Sciences, 2016.765-772.

Baek, M. H. and Kim, T. H. 2015. A study on the use of planarity for quick identification of potential landslide hazard. *Natural Hazards and Earth System Sciences,* 15(5), 997-1009, doi:10.5194/nhess-15-997-2015.

Barnea, S. and Filin, S. 2008. Keypoint based autonomous registration of terrestrial laser point-clouds. *ISPRS Journal of Photogrammetry and Remote Sensing,* 63(1), 19-35, doi:10.1016/j.isprsjprs.2007.05.005.

Brasington, J., Langham, J. and Rumsby, B. 2003. Methodological sensitivity of morphometric estimates of coarse fluvial sediment transport. *Geomorphology,* 53(3-4), 299-316, doi:10.1016/S0169-555X(02)00320-3.

Carbonneau, P. E. and Dietrich, J. T. 2016. Cost-effective non-metric photogrammetry from consumer-grade sUAS: Implications for direct georeferencing of structure from motion photogrammetry. *Earth Surface Processes and Landforms*, doi:10.1002/esp.4012.

Chambers, J. E., Wilkinson, P. B., Kuras, O., Ford, J. R., Gunn, D. A., Meldrum, P. I., Pennington, C. V. L., Weller, A. L., Hobbs, P. R. N. and Ogilvy, R. D. 2011. Three-dimensional geophysical anatomy of an active landslide in Lias Group mudrocks, Cleveland Basin, UK. *Geomorphology,* 125(4), 472-484, doi:10.1016/j.geomorph.2010.09.017.

Cook, K. L. 2017. An evaluation of the effectiveness of low-cost UAVs and structure from motion for geomorphic change detection. *Geomorphology,* 278, 195-208, doi:10.1016/j.geomorph.2016.11.009.

Cruden, D. M. and Varnes, D. J. 1996. Landslide types and processes. *In:* TURNER AK, S. R. (ed.) *Landslides, investigation and mitigation.* Washington, DC. 36-75.

d'Oleire-Oltmanns, S., Marzolff, I., Peter, K. D. and Ries, J. B. 2012. Unmanned Aerial Vehicle (UAV) for monitoring soil erosion in Morocco. *Remote Sensing,* 4(12)**,** 3390-3416, doi:10.3390/rs4113390.

Dall'Asta, E., Forlani, G., Roncella, R., Santise, M., Diotri, F. and Morra di Cella, U. 2017. Unmanned Aerial Systems and DSM matching for rock glacier monitoring. *ISPRS Journal of Photogrammetry and Remote Sensing,* 127(1), doi:10.1016/j.isprsjprs.2016.10.003.

Dellinger, F., Delon, J., Gousseau, Y., Michel, J. and Tupin, F. 2015. SAR-SIFT: A SIFT-like algorithm for SAR images. *IEEE Transactions on Geoscience and Remote Sensing,* 53(1)**,** 453-466, doi:10.1109/TGRS.2014.2323552.

Eltner, A., Kaiser, A., Castillo, C., Rock, G., Neugirg, F. and Abellán, A. 2016. Image-based surface reconstruction in geomorphometry-merits, limits and developments. *Earth Surface Dynamics,* 4(2)**,** 359-389, doi:10.5194/esurf-4-359-2016.

Eltner, A. and Schneider, D. 2015. Analysis of different methods for 3D reconstruction of natural surfaces from parallel-axes UAV images. *The Photogrammetric Record,* 30(151)**,** 279-299, doi:10.1111/phor.12115.

Fieber, K. D., Mills, J. P., Miller, P. E., Clarke, L., Ireland, L. and Fox, A. J. 2018. Rigorous 3D change determination in Antarctic Peninsula glaciers from stereo WorldView-2 and archival aerial imagery. *Remote Sensing of Environment,* 205**,** 18-31, doi:10.1016/j.rse.2017.10.042.

Fischler, M. A. and Bolles, R. C. 1981. Random sample consensus: a paradigm for model fitting with applications to image analysis and automated cartography. *Communications of the ACM,* 24(6)**,** 381-395, doi:10.1145/358669.358692.

Fonstad, M. A., Dietrich, J. T., Courville, B. C., Jensen, J. L. and Carbonneau, P. E. 2013. Topographic structure from motion: A new development in photogrammetric measurement. *Earth Surface Processes and Landforms,* 38(4)**,** 421-430, doi:10.1002/esp.3366.

Gerke, M. and Przybilla, H. J. 2016. Accuracy analysis of photogrammetric UAV image blocks: Influence of onboard RTK-GNSS and cross flight patterns. *Photogrammetrie, Fernerkundung, Geoinformation,* 2016(1)**,** 17-30, doi:10.1127/pfg/2016/0284.

Gneeniss, A. S., Mills, J. P. and Miller, P. E. 2015. In-flight photogrammetric camera calibration and validation via complementary lidar. *ISPRS Journal of*

Photogrammetry and Remote Sensing, 100**,** 3-13, doi:10.1016/j.isprsjprs.2014.04.019.

Gonçalves, J. A. and Henriques, R. 2015. UAV photogrammetry for topographic monitoring of coastal areas. *ISPRS Journal of Photogrammetry and Remote Sensing,* 104**,** 101-111, doi:10.1016/j.isprsjprs.2015.02.009.

Gray, A. 1997. The Three Fundamental Forms. *Modern Differential Geometry of Curves and Surfaces with Mathematica.* 2nd ed.: CRC Press, Inc. 1056.

Haque, U., Blum, P., da Silva, P. F., Andersen, P., Pilz, J., Chalov, S. R., Malet, J. P., Auflič, M. J., Andres, N., Poyiadji, E., Lamas, P. C., Zhang, W., Peshevski, I., Pétursson, H. G., Kurt, T., Dobrev, N., García-Davalillo, J. C., Halkia, M., Ferri, S., Gaprindashvili, G., Engström, J. and Keellings, D. 2016. Fatal landslides in Europe. *Landslides,* 13(6)**,** 1545-1554, doi:10.1007/s10346-016-0689-3.

Immerzeel, W. W., Kraaijenbrink, P. D. A., Shea, J. M., Shrestha, A. B., Pellicciotti, F., Bierkens, M. F. P. and De Jong, S. M. 2014. High-resolution monitoring of Himalayan glacier dynamics using unmanned aerial vehicles. *Remote Sensing of Environment,* 150**,** 93-103, doi:10.1016/j.rse.2014.04.025.

Jaboyedoff, M., Oppikofer, T., Abellán, A., Derron, M. H., Loye, A., Metzger, R. and Pedrazzini, A. 2012. Use of LIDAR in landslide investigations: A review. *Natural Hazards,* 61(1)**,** 5-28, doi:10.1007/s11069-010-9634-2.

James, M. R. and Robson, S. 2012. Straightforward reconstruction of 3D surfaces and topography with a camera: Accuracy and geoscience application. *Journal of Geophysical Research: Earth Surface,* 117(3), doi:10.1029/2011jf002289.

James, M. R. and Robson, S. 2014. Mitigating systematic error in topographic models derived from UAV and ground-based image networks. *Earth Surface Processes and Landforms,* 39(10)**,** 1413-1420, doi:10.1002/esp.3609.

James, M. R., Robson, S., d'Oleire-Oltmanns, S. and Niethammer, U. 2017a. Optimising UAV topographic surveys processed with structure-from-motion: Ground control quality, quantity and bundle adjustment. *Geomorphology,* 280**,** 51-66, doi:10.1016/j.geomorph.2016.11.021.

James, M. R., Robson, S. and Smith, M. W. 2017b. 3-D uncertainty-based topographic change detection with structure-from-motion photogrammetry: precision maps for ground control and directly georeferenced surveys [in press]. *Earth Surface Processes and Landforms* doi:10.1002/esp.4125.

Lague, D., Brodu, N. and Leroux, J. 2013. Accurate 3D comparison of complex topography with terrestrial laser scanner: Application to the Rangitikei canyon (N-Z). *ISPRS Journal of Photogrammetry and Remote Sensing,* 82**,** 10-26, doi:10.1016/j.isprsjprs.2013.04.009.

Lane, S. N., Westaway, R. M. and Hicks, D. M. 2003. Estimation of erosion and deposition volumes in a large, gravel-bed, braided river using synoptic remote sensing. *Earth Surface Processes and Landforms,* 28(3)**,** 249-271, doi:10.1002/esp.483.

Lowe, D. G. 2004. Distinctive image features from scale-invariant keypoints. *International Journal of Computer Vision,* 60(2)**,** 91-110, doi:10.1023/B:VISI.0000029664.99615.94.

Niethammer, U., James, M. R., Rothmund, S., Travelletti, J. and Joswig, M. 2012. UAV-based remote sensing of the Super-Sauze landslide: Evaluation and results. *Engineering Geology,* 128**,** 2-11, doi:10.1016/j.enggeo.2011.03.012.

Peppa, M. V., Mills, J. P., Moore, P., Miller, P. E. and Chambers, J. E. 2016. Accuracy assessment of a uav-based landslide monitoring system. The International Archives of the Photogrammetry, Remote Sensing and Spatial Information Sciences, 2016.895-902.

Pfeifer, N., Mandlburger, G., Otepka, J. and Karel, W. 2014. OPALS: A framework for Airborne Laser Scanning data analysis. *Computers, Environment and Urban Systems,* 45**,** 125-136, doi:10.1016/j.compenvurbsys.2013.11.002.

PhotoScan. 2016. Commercial SfM and image matching software from Russian company Agisoft version 1.2.5 (www.agisoft.com). Available: User's manual (http://www.agisoft.com/downloads/user-manuals/) [Accessed 15th March 2017].

QuestUAV, 2017. *Quest-300 UAV specifications* [Online]. Available: http://www.questuav.co.uk/images/Q300_spec.pdf [Accessed: 12th December, 2017].

Rehak, M. and Skaloud, J. 2017. Time synchronization of consumer cameras on Micro Aerial Vehicles. *ISPRS Journal of Photogrammetry and Remote Sensing,* 123**,** 114-123, doi:10.1016/j.isprsjprs.2016.11.009.

Remondino, F., Spera, M. G., Nocerino, E., Menna, F. and Nex, F. 2014. State of the art in high density image matching. *The Photogrammetric Record,* 29(146)**,** 144-166, doi:10.1111/phor.12063.

Reshetyuk, Y. and Mårtensson, S. G. 2016. Generation of Highly Accurate Digital Elevation Models with Unmanned Aerial Vehicles. *The Photogrammetric Record,* 31(154), 143-165, doi:10.1111/phor.12143.

Rigol-Sanchez, J. P., Stuart, N. and Pulido-Bosch, A. 2015. ArcGeomorphometry: A toolbox for geomorphometric characterisation of DEMs in the ArcGIS environment. *Computers and Geosciences,* 85, 155-163, doi:10.1016/j.cageo.2015.09.020.

Scaioni, M., Longoni, L., Melillo, V. and Papini, M. 2014. Remote sensing for landslide investigations: An overview of recent achievements and perspectives. *Remote Sensing,* 6(10), 9600-9652, doi:10.3390/rs6109600.

Sima, A. A., Buckley, S. J., Kurz, T. H. and Schneider, D. 2014. Semi-automated registration of close-range hyperspectral scans using oriented digital camera imagery and a 3D model. *The Photogrammetric Record,* 29(145), 10-29, doi:10.1111/phor.12049.

Snavely, N., Seitz, S. M. and Szeliski, R. 2008. Modeling the world from Internet photo collections. *International Journal of Computer Vision,* 80(2), 189-210, doi:10.1007/s11263-007-0107-3.

Tarolli, P. 2014. High-resolution topography for understanding Earth surface processes: Opportunities and challenges. *Geomorphology,* 216, 295-312, doi:10.1016/j.geomorph.2014.03.008.

Travelletti, J., Delacourt, C., Allemand, P., Malet, J. P., Schmittbuhl, J., Toussaint, R. and Bastard, M. 2012. Correlation of multi-temporal ground-based optical images for landslide monitoring: Application, potential and limitations. *ISPRS Journal of Photogrammetry and Remote Sensing,* 70, 39-55, doi:10.1016/j.isprsjprs.2012.03.007.

Turner, I. L., Harley, M. D. and Drummond, C. D. 2016. UAVs for coastal surveying. *Coastal Engineering,* 114, 19-24, doi:10.1016/j.coastaleng.2016.03.011.

Uhlemann, S., Chambers, J., Wilkinson, P., Maurer, H., Merritt, A., Meldrum, P., Kuras, O., Gunn, D., Smith, A. and Dijkstra, T. 2017. Four-dimensional imaging of moisture dynamics during landslide reactivation. *Journal of Geophysical Research: Earth Surface,* 122(1), 398-418, doi:10.1002/2016JF003983.

Uhlemann, S., Smith, A., Chambers, J., Dixon, N., Dijkstra, T., Haslam, E., Meldrum, P., Merritt, A., Gunn, D. and Mackay, J. 2016. Assessment of ground-based monitoring techniques applied to landslide investigations. *Geomorphology,* 253, 438-451, doi:10.1016/j.geomorph.2015.10.027.

Wang, L., Niu, Z., Wu, C., Xie, R. and Huang, H. 2012. A robust multisource image automatic registration system based on the SIFT descriptor. *International Journal of Remote Sensing,* 33(12), 3850-3869, doi:10.1080/01431161.2011.636079.

Wheaton, J. M., Brasington, J., Darby, S. E. and Sear, D. A. 2010. Accounting for uncertainty in DEMs from repeat topographic surveys: Improved sediment budgets. *Earth Surface Processes and Landforms,* 35(2), 136-156, doi:10.1002/esp.1886.

Woodget, A. S., Carbonneau, P. E., Visser, F. and Maddock, I. P. 2015. Quantifying submerged fluvial topography using hyperspatial resolution UAS imagery and structure from motion photogrammetry. *Earth Surface Processes and Landforms,* 40(1), 47-64, doi:10.1002/esp.3613.

Wu, C. 2014. Critical Configurations for Radial Distortion Self-Calibration. 2014 IEEE Conference on Computer Vision and Pattern Recognition, 23-28 June 2014 2014.25-32.

Wujanz, D., Krueger, D. and Neitzel, F. 2016. Identification of Stable Areas in Unreferenced Laser Scans for Deformation Measurement. *The Photogrammetric Record,* 31(155), 261-280, doi:10.1111/phor.12152.

Yokoyama, R., Shirasawa, M. and Pike, R. J. 2002. Visualizing topography by openness: A new application of image processing to digital elevation models. *Photogrammetric Engineering and Remote Sensing,* 68(3), 257-265.

Table 1: Specifications of Panasonic Lumix DMC-LX5 and Sony A6000.

	Panasonic Lumix DMC-LX5	Sony A6000
Lens type	Leica Vario-Summicron	Sony E F2.8 pancake-
Nominal focal length (35 mm equivalent) [mm]	5.1 (24.0-90.0)	16.0 (24.0)
Sensor type and size [mm]	CCD, 8.07 x 5.56	APS-C CMOS, 23.5 x 15.6
Maximum image resolution [pixels]	3648 x 2736	6000 x 4000
Pixel size [μm]	2.0 x 2.0	3.9 x 3.9

Table 2: Sandford test site: Statistics of coordinate residuals of the MBR-derived pseudo GCPs.

Epoch	Pseudo GCPs	Easting [m]			Northing [m]			Elevation [m]		
		mean	σ	RMSE	mean	σ	RMSE	mean	σ	RMSE
E1	94	0.006	0.019	0.020	0.000	0.021	0.021	0.002	0.030	0.030
E2	102	0.050	0.021	0.022	0.070	0.020	0.028	-0.050	0.020	0.020

Table 3: Sandford test site: RMSEs and sensitivity estimations of the GCP-based and MBR-GCP experiments.

	GCP-based Panasonic [m]					MBR-GCP Panasonic [m]				
Epoch	RMSE of M3C2 comparison against TLS	3D RMSE at CPs (e_{geor})	RMSE of M3C2 comparison after ICP ($e_{co\text{-}reg}$)	s_1	s_2	RMSE of M3C2 comparison against TLS	3D RMSE at CPs (e_{geor})	RMSE of M3C2 comparison after ICP ($e_{co\text{-}reg}$)	s_1	s_2
E0		0.030								
E1	0.045	0.029	0.050	0.082	0.114	0.049	0.035	0.046	0.090	0.107
E2	0.043	0.024	0.042	0.075	0.099	0.045	0.050	0.040	0.115	0.098

Table 4: Sandford test site: Statistics of elevation differences of epoch pair E2-E0 over area of slope failure.

Experiment	μ [m]	σ [m]	RMSE [m]	Minimum [m]	Maximum [m]
TLS	0.10	0.58	0.58	-0.77	1.17
GCP-based	0.12	0.52	0.53	-0.74	1.02
MBR-GCP	0.09	0.52	0.53	-0.76	0.99

Table 5: Sandford test site: Volume changes for epoch pair E2-E0 over area of slope failure.

Experiment	Cut [m^3]	Fill [m^3]	Net [m^3]
TLS	-10.14 ± 2.62	15.26 ± 3.28	5.12 ± 4.20
GCP-based	-8.63 ± 2.40	14.20 ± 3.30	5.57 ± 4.08
MBR-GCP	-9.27 ± 2.55	13.52 ± 3.28	4.25 ± 4.04

Table 6: Hollin Hill landslide: Details of UAV data processing.

Campaign (month/year)	Epoch	No of Images	No GCPs	No CPs	GSD[m]	Average flying height [m]	Average point cloud density [points/m^2]
Panasonic Lumix DMC-LX5							
12/14	E0	67	5	5	0.034	108	214
03/15	E1	200	5	6	0.030	87	271
06/15	E2	257	5	13	0.031	87	265
09/15	E3	197	5	15	0.028	83	314
02/16	E4	195	5	15	0.028	90	309
05/16	E5	189	5	15	0.029	84	292
Sony A6000							
02/16	E4	144	5	15	0.018	79	761
05/16	E5	221	5	15	0.019	82	717

Table 7: Hollin Hill landslide: Statistics of coordinate residuals of the MBR-derived pseudo GCPs.

Experi-ment	Epoch	Pseudo GCPs	Easting [m]			Northing [m]			Elevation [m]		
			mean	σ	RMSE	mean	σ	RMSE	mean	σ	RMSE
MBR-GCP Panasonic	E1	1096	0.002	0.023	0.023	0.001	0.019	0.019	0.001	0.028	0.028
	E2	743	0.006	0.029	0.029	-0.003	0.035	0.035	-0.004	0.018	0.018
	E3	541	-0.019	0.034	0.039	0.018	0.034	0.038	-0.002	0.020	0.021
	E4	654	0.001	0.021	0.021	0.000	0.027	0.027	0.000	0.016	0.016
	E5	1298	-0.004	0.050	0.050	0.008	0.050	0.050	0.002	0.029	0.029
MBR-GCP Sony	E5	37	0.004	0.035	0.035	-0.012	0.038	0.039	-0.005	0.030	0.030
MBR-UAV Sony	E5	28	-0.023	0.035	0.041	0.025	0.035	0.043	-0.031	0.034	0.045

Table 8: Hollin Hill landslide: Sensitivity estimations of the GCP-based and MBR-GCP Panasonic experiments.

	GCP-based Panasonic [m]				MBR-GCP Panasonic [m]			
Epoch	3D RMSE at CPs (e_{geor})	RMSE of M3C2 comparison after ICP ($e_{co\text{-}reg}$)	s_1	s_2	3D RMSE at CPs (e_{geor})	RMSE of M3C2 comparison after ICP ($e_{co\text{-}reg}$)	s_1	s_2
E0	0.033							
E1	0.024	0.018	0.079	0.073	0.071	0.108	0.153	0.221
E2	0.036	0.019	0.096	0.074	0.075	0.031	0.161	0.088
E3	0.045	0.027	0.109	0.083	0.067	0.055	0.147	0.126
E4	0.022	0.017	0.078	0.072	0.086	0.041	0.180	0.103
E5	0.029	0.030	0.085	0.087	0.108	0.087	0.221	0.182

Table 9: Hollin Hill landslide: Sensitivity estimations of the GCP-based, MBR-GCP and MBR-UAV Sony experiments.

	GCP-based Sony [m]				MBR-GCP Sony [m]				MBR-UAV Sony [m]	
Epoch	3D RMSE at CPs (e_{geor})	RMSE of M3C2 comparison after ICP ($e_{co\text{-}reg}$)	s_1	s_2	3D RMSE at CPs (e_{geor})	RMSE of M3C2 comparison after ICP ($e_{co\text{-}reg}$)	s_1	s_2	RMSE of M3C2 comparison after ICP ($e_{co\text{-}reg}$)	s_2
E4	0.037									
E5	0.028	0.057	0.091	0.133	0.066	0.090	0.148	0.19	0.078	0.153

Table 10: Hollin Hill landslide: Elevations differences between experimental results and independently observed elevations at spot heights in E5.

Experiments	mean [m]	Vertical RMSE [m]
GCP-based Panasonic	0.003	0.088
MBR-GCP Panasonic	-0.014	0.104
GCP-based Sony	0.004	0.081
MBR-GCP Sony	0.010	0.089

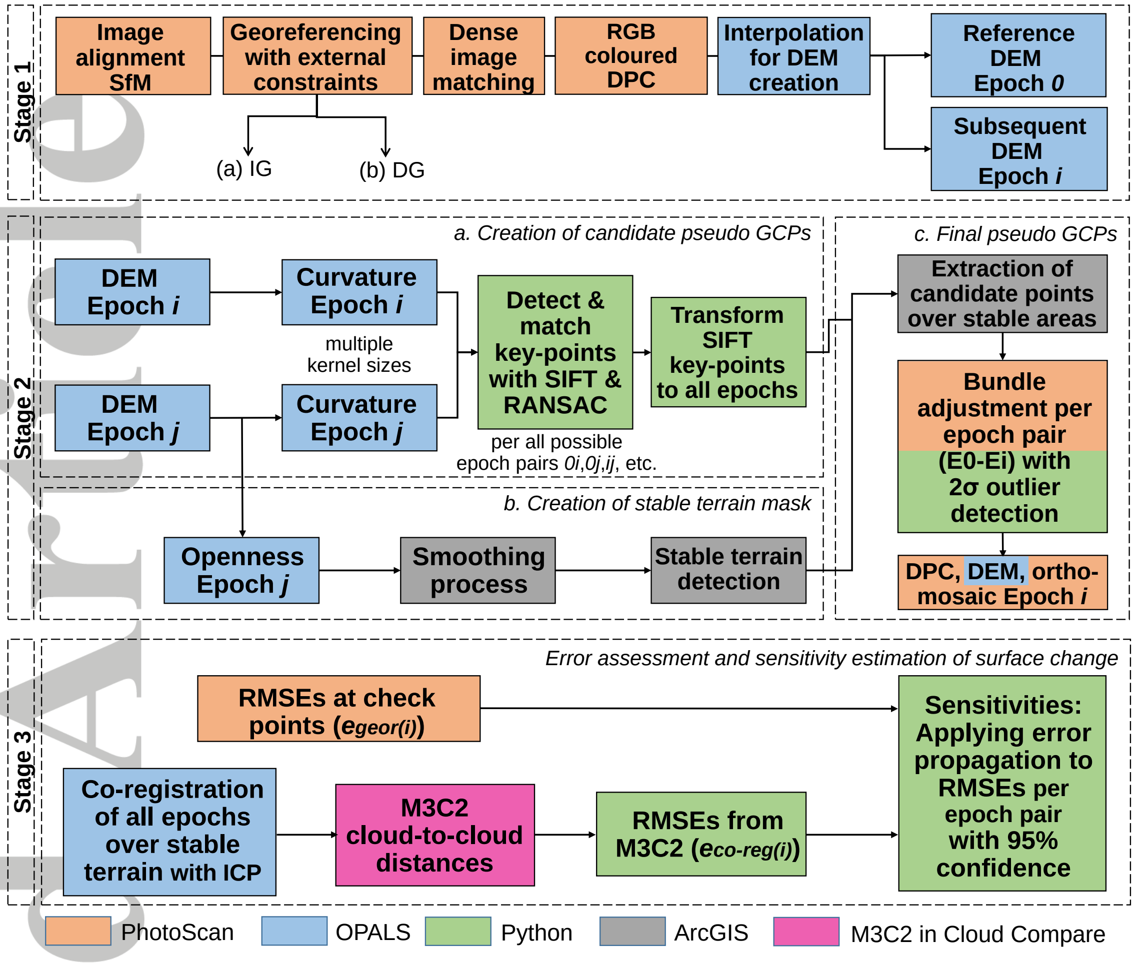

Figure 1: Workflow of the MBR approach to generate a UAV-derived time series of SfM-MVS outputs.

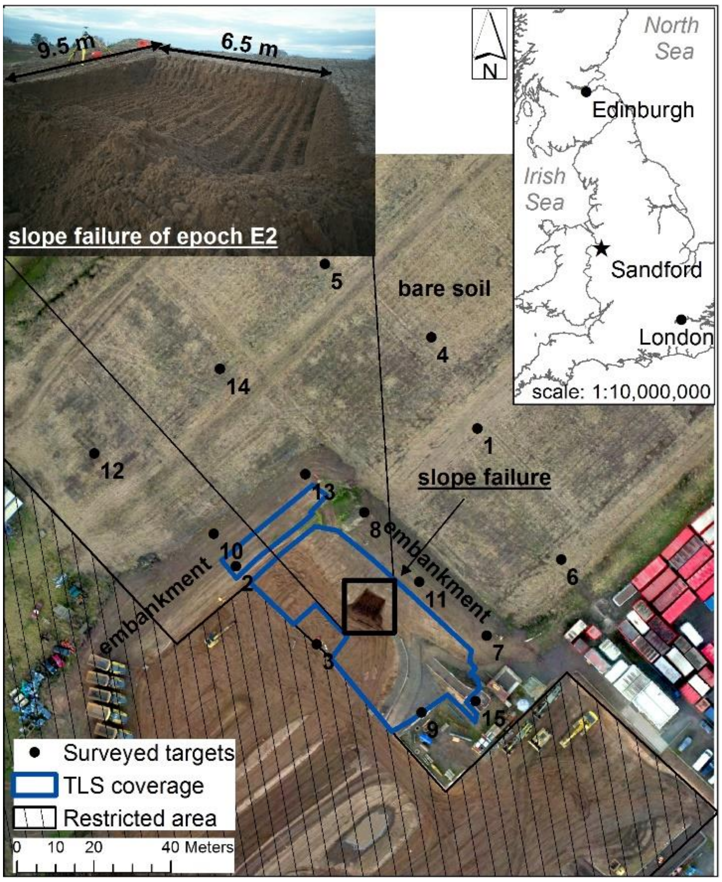

Figure 2: Overview of the Sandford Industrial Park test site.

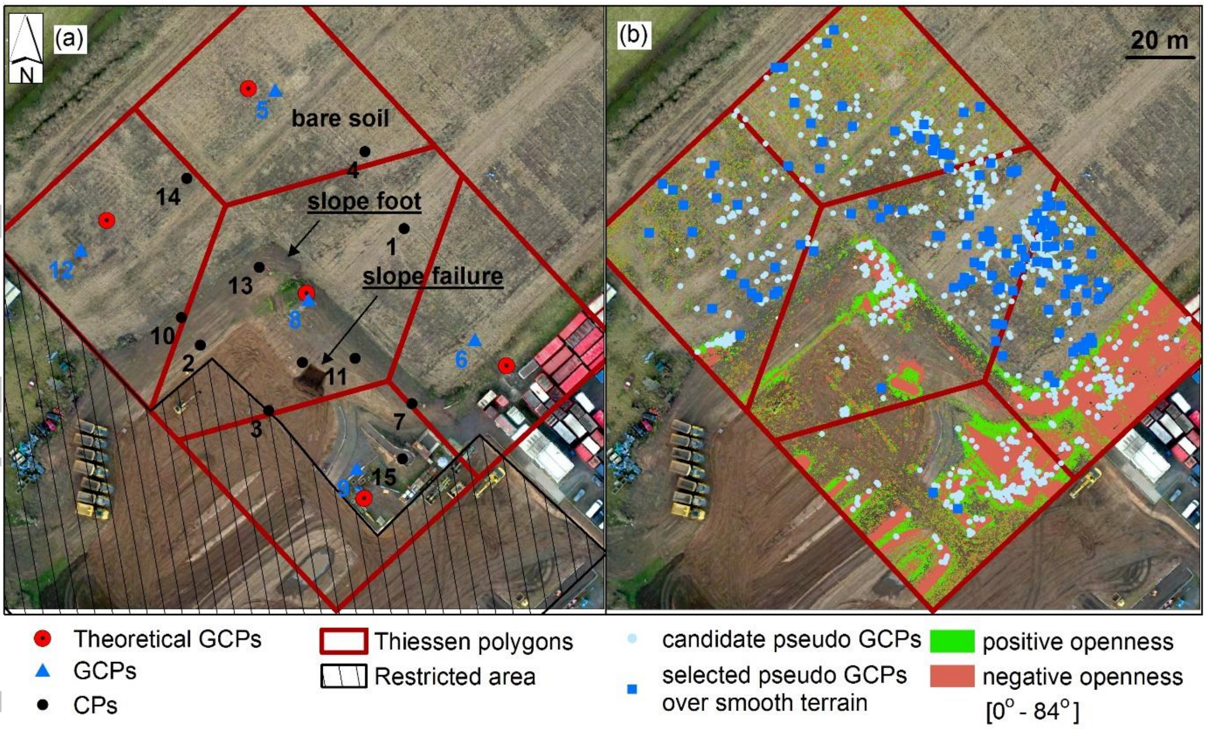

Figure 3: Sandford test site: (a) Distribution of GCPs and CPs for the GCP-based experiment. (b) Overview of openness grids together with the generated pseudo GCPs.

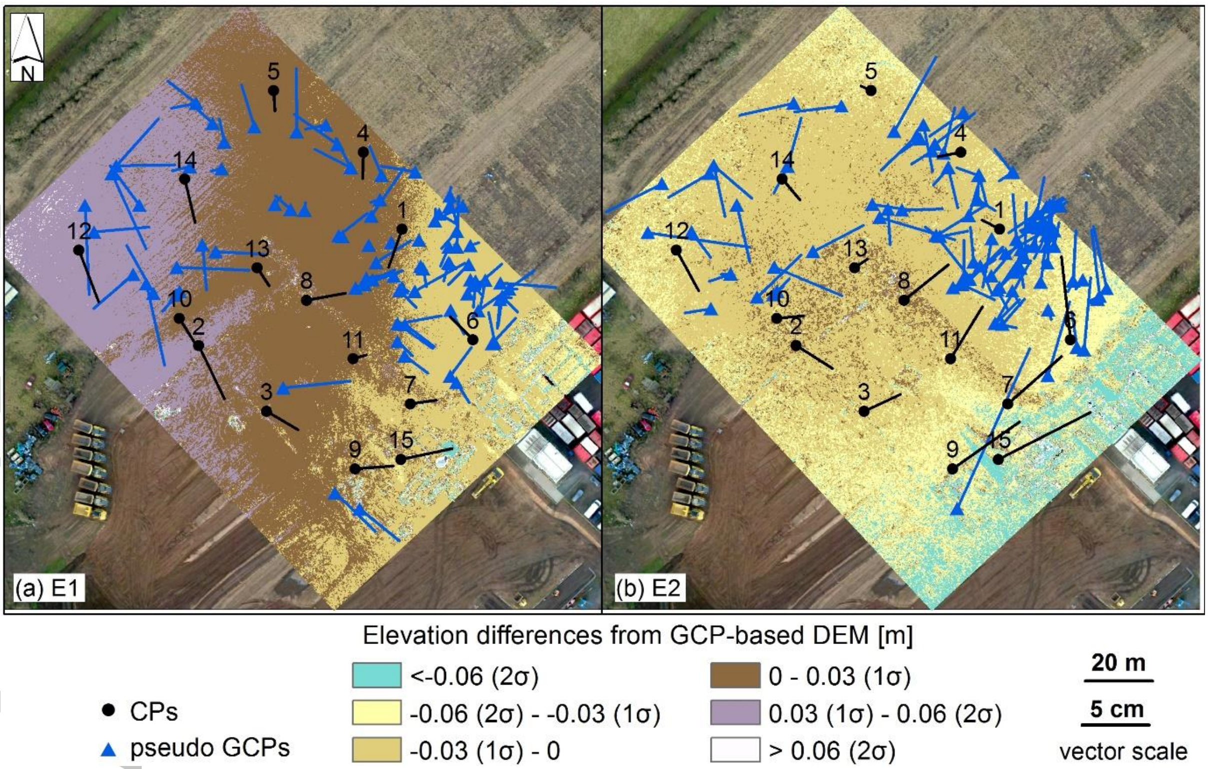

Figure 4: Sandford test site: Elevation differences between GCP-based and MBR-GCP DEMs of (a) E1 and (b) E2 epochs.

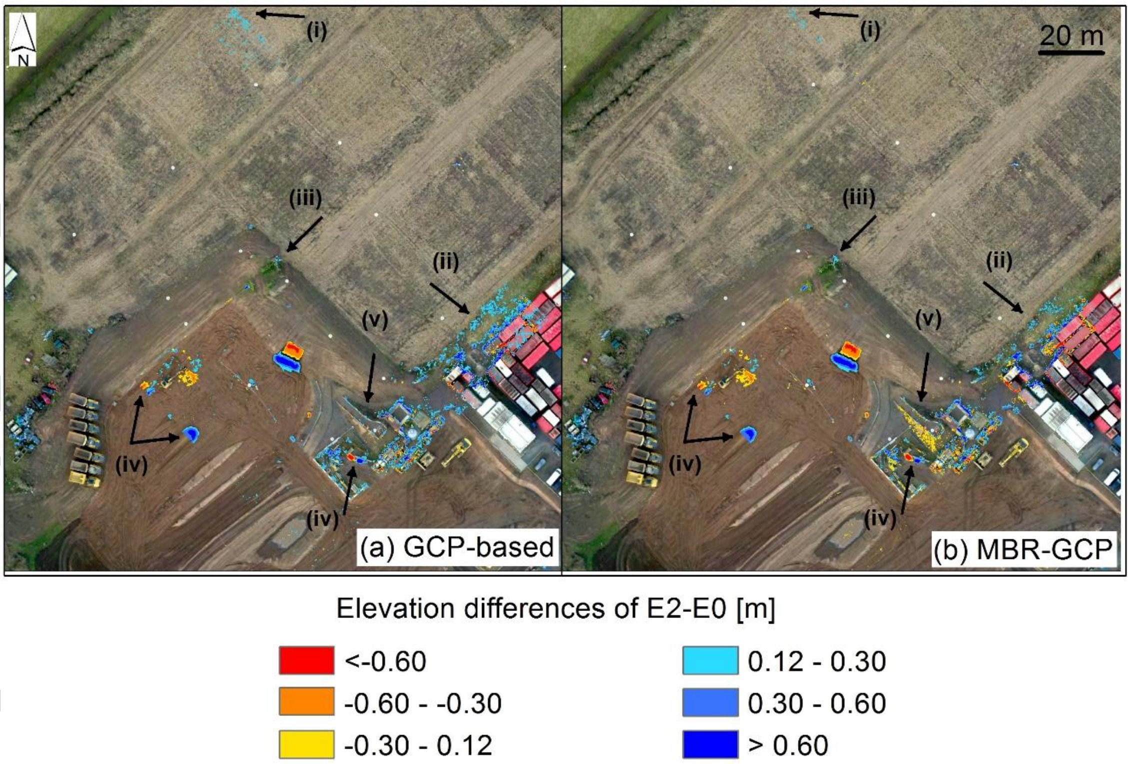

Figure 5: Sandford test site: Elevation differences of E2-E0 epoch pair derived from (a) GCP-based and (b) MBR-GCP experiments.

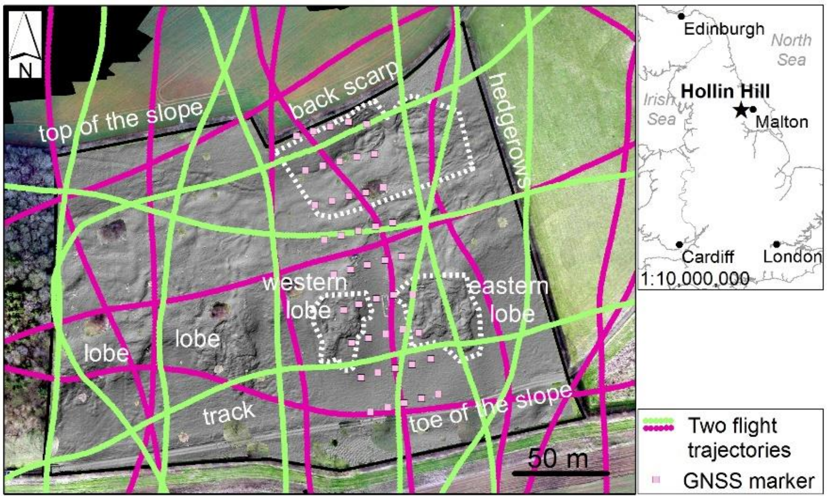

Figure 6: Hollin Hill landslide: Shaded relief illustrating two E5 flight trajectories.

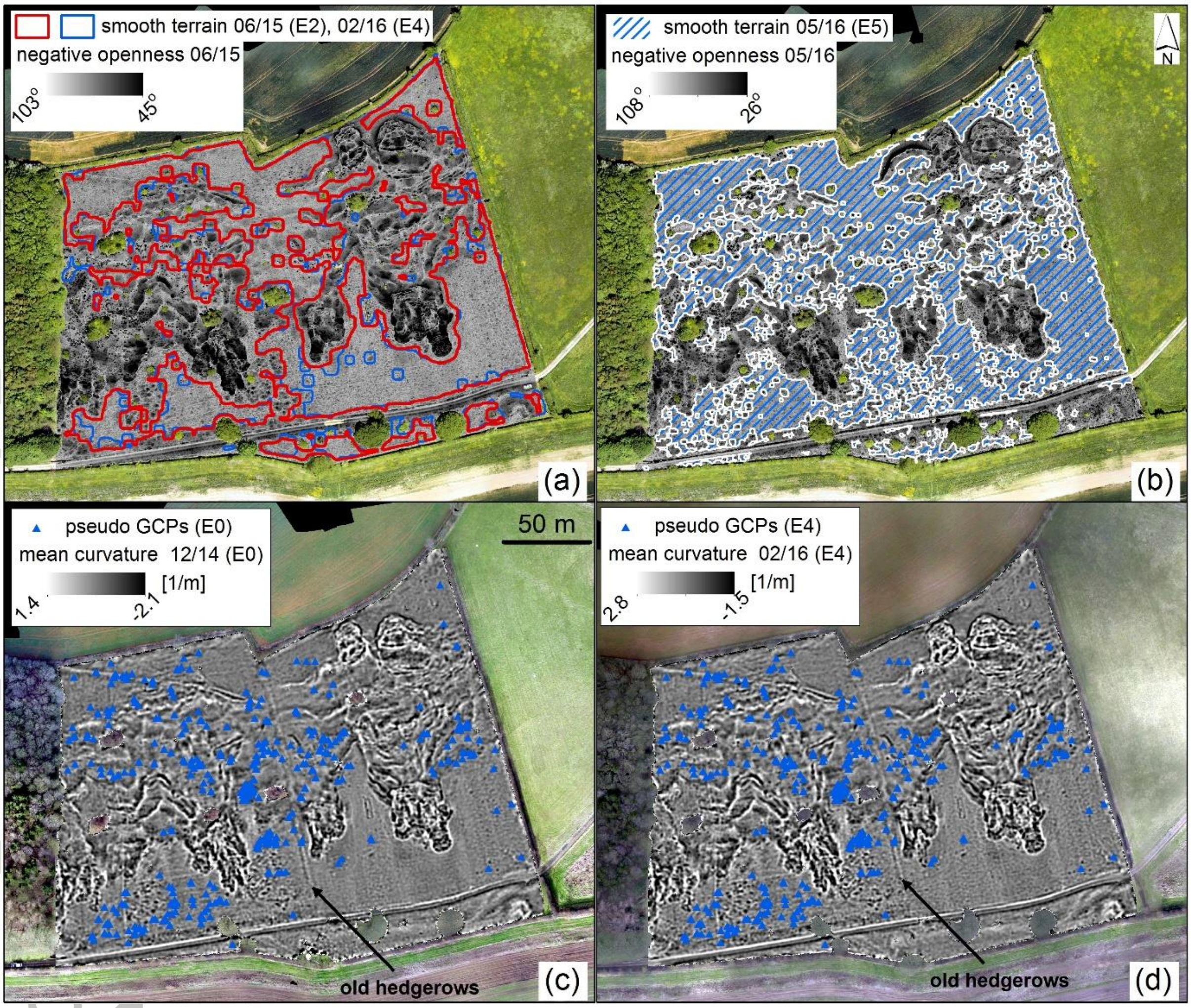

Figure 7: Hollin Hill landslide: Negative openness for stable terrain extraction of (a) E2, E4 and (b) E5 epochs. Mean curvature of (c) E0 and (d) E4 epochs with their corresponding pseudo GCPs over stable terrain.

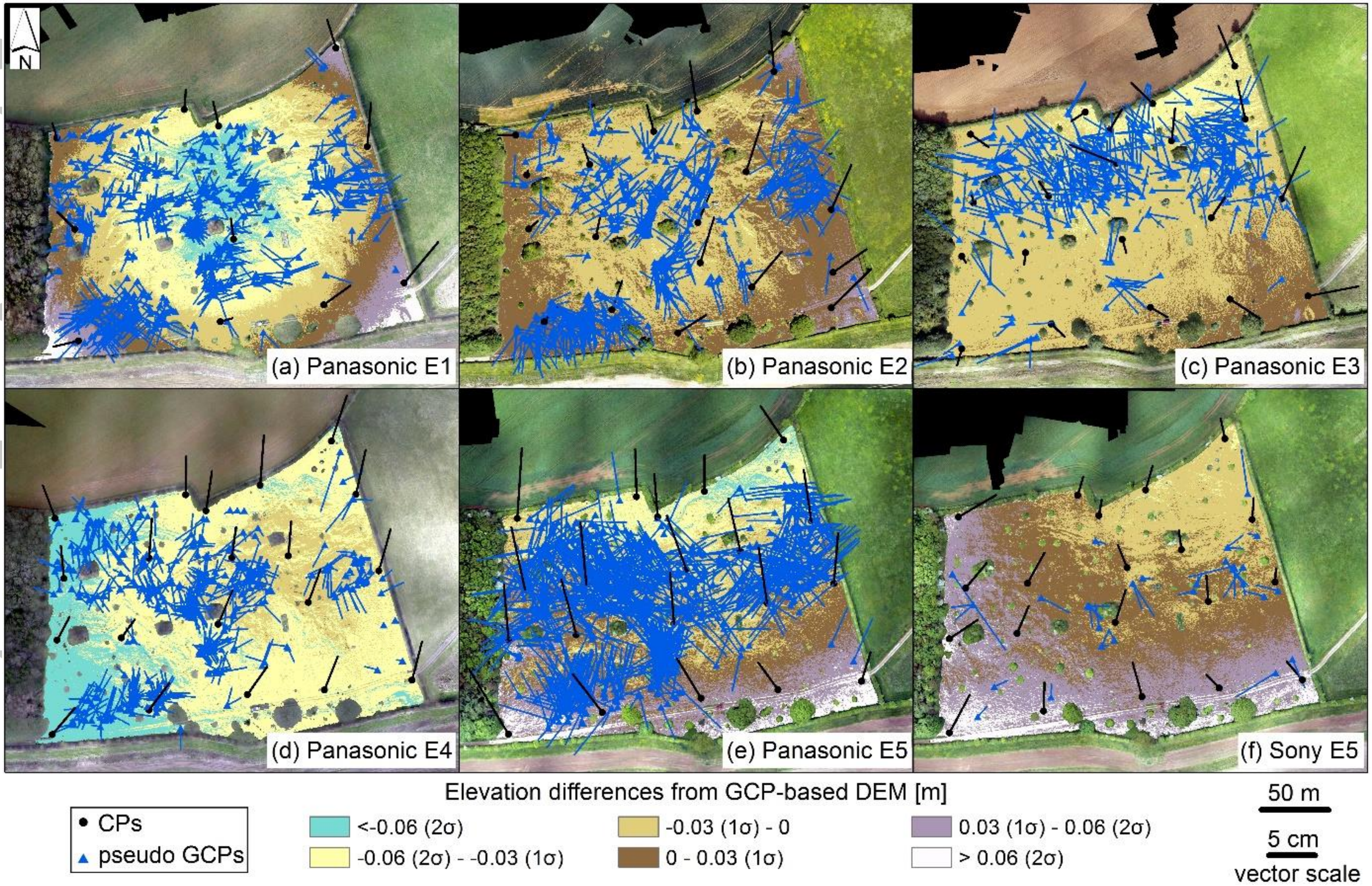

Figure 8: Hollin Hill landslide: Planimetric error vectors of pseudo GCPs and CPs with elevation differences between GCP-based and MBR-GCP (a)-(e) Panasonic and (f) Sony outputs.

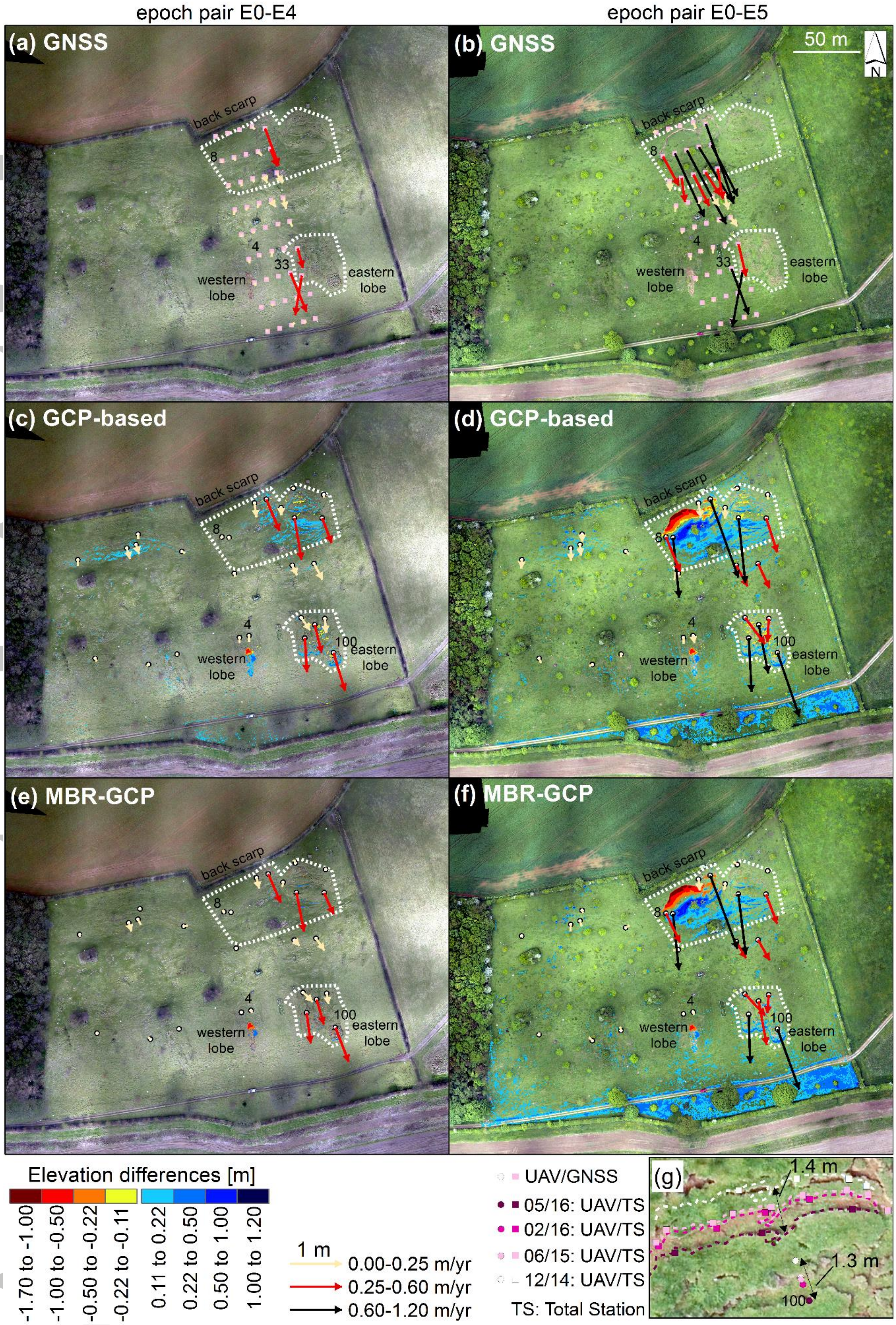

Figure 9: Hollin Hill landslide: Elevation differences and planimetric vectors indicating the horizontal 2D displacement rate of E0-E4 and E0-E5 epoch pairs derived from (a, b) GNSS, (c, d) GCP-based and (e, f) MBR-GCP Panasonic observations as well as planimetric movement from (g) total station.

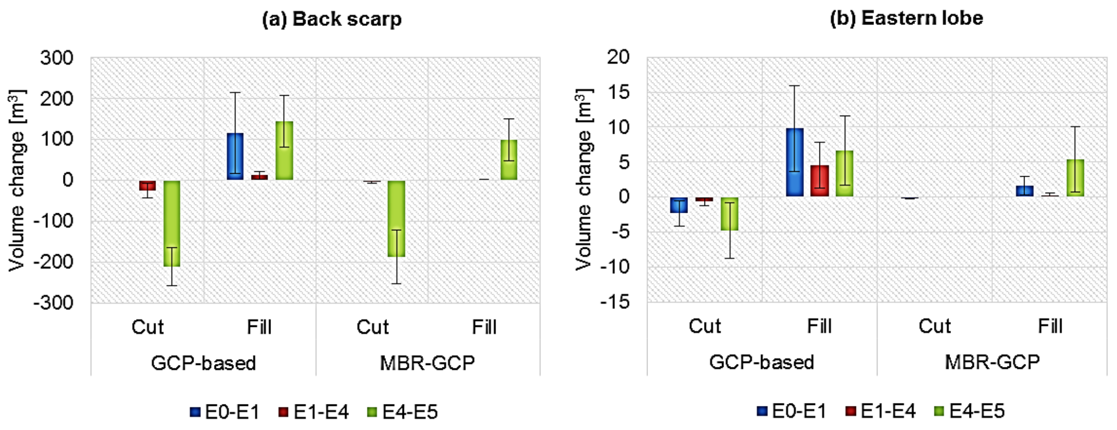

Figure 10: Hollin Hill: Volume change over (a) back scarp and (b) eastern lobe for three epoch pairs computed by GCP-based and MBR-GCP Panasonic elevation differences.

Automated co-registration and calibration in SfM photogrammetry for landslide change detection

M. V. Peppa*, J. P. Mills, P. Moore, P. E. Miller, J. E. Chambers

An automated co-registration and calibration SfM photogrammetric workflow, namely Morphology-based co-Registration (MBR), enables the rigorous alignment of spatio-temporal UAV-derived observations in the absence of physically established ground control points and quantifies landslide kinematics. It is based on the implementation of the SIFT-RANSAC algorithm with the morphological attributes of curvature and openness to generate pseudo control points over stable terrain in conjunction with the SfM-MVS pipeline. This UAV-based SfM photogrammetric strategy constitutes a potential time-efficient and cost-effective approach for landslide change detection, beneficial for inaccessible and hazardous areas.